THE JOURNAL OF PHYSICAL CHEMISTRY C
A JOURNAL OF THE AMERICAN CHEMICAL SOCIETY

pubs.acs.org/JPCC
Article

Impact of Chloride and Bromide Composition in Ionic Liquid/Water Electrolytes on the Electrochemical Performance of Graphene-Based Supercapacitors: A Molecular Dynamics Study

Leonardo B. A. Oliveira, Lucas de S Silva, Henrique de Araujo Chagas, Tertius L. Fonseca, and Guilherme Colherinhas*

Cite This: J. Phys. Chem. C 2025, 129, 13532−13541
Read Online

ACCESS | Metrics & More | Article Recommendations | Supporting Information

ABSTRACT: The electrochemical performance of supercapacitors (SCs) is significantly influenced by the composition of their electrolytes. In this study, we investigate the effects of chloride ($[Cl]^-$) and bromide ($[Br]^-$) anion variations in 1-butyl-3-methylimidazolium $[bmim]^+$/water mixtures for graphene-based SCs using atomistic molecular dynamics simulations. We analyze the structural and energetic profiles of the electrical double layer (EDL), focusing on ion and water distributions, electrostatic charge profiles, and interaction energies at charged electrode interfaces. The results reveal that $[Cl]^-$ and $[Br]^-$ variations have a minimal impact on electrostatic charge distributions but play a crucial role in determining the gravimetric energy density of SCs. Notably, increasing $[Cl^-]$ concentration enhances the gravimetric energy density by approximately 9% without compromising electrochemical stability, which is particularly advantageous for weight-sensitive applications such as portable electronics and electric vehicles. Additionally, we examined the influence of hydration levels, showing that higher water content improves the gravimetric efficiency of the electrolyte. These findings provide valuable insights into optimizing ionic liquid (IL)/water-based electrolytes for high-performance SCs.

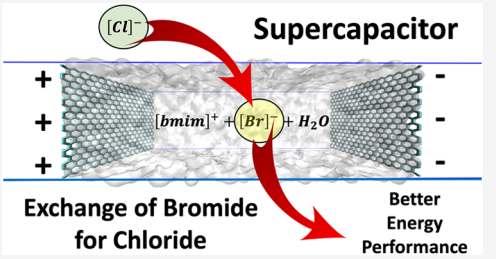

1. INTRODUCTION

Electrolytes play a critical role in the development of efficient electrochemical energy storage (EES) systems, as their properties significantly influence performance.[1−6] Ionic liquids (ILs) are attracting increasing academic and industrial interest as alternatives to organic solvents in catalysis, synthesis, and other applications, in addition to their well-established role in electrochemistry.[7−12] For EES applications, ILs are valued for their excellent thermal and chemical stability, broad compositional variability, and negligible vapor pressure, even at elevated temperatures.[13] However, their high density often limits their ionic conductivity. This limitation can be mitigated by adding suitable cosolvents, such as water or organic solvents, which effectively reduce viscosity. Although water addition can lower viscosity, it can also significantly impact other thermodynamic properties of ILs, such as the electrochemical window and thermal stability.

To date, numerous review articles have addressed various aspects of water in ILs, particularly at electrolyte/electrode interfaces, as the performance of EES systems is governed by electrochemical interfaces.[14−19] Recent studies have explored aqueous ionic liquids of various classes as electrolytes in supercapacitors (SC) to better understand the impact of hydration on key device parameters including ion size and type, surface charge density, electrode materials, and electrolyte concentration. Along these lines, Feng et al.[14] investigated the effects of water adsorption at electrified interfaces in room-temperature ionic liquids (RTILs) using molecular dynamics (MD) simulations. Their findings demonstrated that multiple factors govern water distribution, including interactions with the inhomogeneous electric field, associations with surrounding ions, and the availability of free space near electrodes. These factors work synergistically to create specific water distributions and are strongly influenced by ion characteristics and electrode polarization, explaining ion specificity and polarity asymmetry in water electrosorption. Chen et al.[18] studied how adding Li salt to humid hydrophobic ionic liquids mitigates the water-induced reduction of the electrochemical window. Using MD simulations and cyclic voltammetry, the authors demonstrated that Li salt effectively repels water from electrode surfaces, thereby reducing water's electrochemical activity. More recently, some works[6,13,20−22] systematically analyzed the effects of hydration on the electrical properties of IL-based SCs with graphene or graphyne electrodes. Their results indicated that hydration could enhance the gravimetric

Received: March 18, 2025
Revised: April 27, 2025
Accepted: May 20, 2025
Published: May 26, 2025

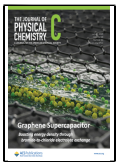

https://doi.org/10.1021/acs.jpcc.5c01816
J. Phys. Chem. C 2025, 129, 13532−13541

energy density and, consequently, improve the SC gravimetric energy storage performance.

Systems incorporating ILs and cosolvents must be carefully designed to account for the influence of IL cations and anions, as well as the type of cosolvent used. Such systems can exhibit exceptional electrolyte properties in SCs, enhancing both the cell voltage and energy storage density. As demonstrated in previous work, small anions such as $[Cl]^-$, $[Br]^-$, and $[I]^-$ are particularly suitable due to their hydration and solvation properties.[23−25] From a fundamental research perspective, the properties of ILs are primarily governed by electrostatic interactions and hydrogen bonding (HB). Introducing cosolvents with varying dielectric constants or polarities provides valuable insights into their effects on the microstructural behavior of ILs. This study suggests that replacing bromide $[Br]^-$ with chloride $[Cl]^-$ in 1-butyl-3-methylimidazolium $[bmim]^+/H_2O$ mixtures with a constant water concentration can further improve electrolyte performance in SCs by expanding the range of applicable electrolytes.

2. METHODOLOGY

The effect of varying $[Cl]^-$ and $[Br]^-$ concentrations in ILs/water electrolytes for graphene-based SCs is investigated through classical atomistic MD simulations. Five different ILs/water electrolytes were analyzed: $w[bmim]^+ + n[Cl]^- + m[Br]^- + x[H_2O]$, with $w = n + m$ and $(n, m) = (0, 100\%)$; $(25, 75\%)$; $(50, 50\%)$; $(75, 25\%)$; or $(100, 0\%)$. The total amount of $[Cl]^-$ or $[Br]^-$ ions present in the solution must exactly match the total amount of $[bmim]^+$ ions (250 for all models), implying an ionic solution with a net zero charge. For the hydration of the electrolytes, we adopted the same strategy outlined in a previous study.[21] The water/IL ratio of approximately 12 (around 60% hydration) was chosen based on previous studies to balance viscosity and ionic conductivity.[21] This ratio was kept constant across systems, causing small variations in the water molecule count but maintaining component proportions. This ensures consistent analysis of ionic interactions and the EDL structure (see Table 1 for compositions of all five models). Figure 1 shows the structures of the graphene electrode used in MD simulation and each ionic compound in the composition of the electrolyte of the SCs.

Table 1. Composition of the Electrolytes Investigated in This Work ($w = n + m$)

electrolyte $w[bmim]^+ + n[Cl]^- + m[Br]^- + x[H_2O]$	[bmim][Cl] # pairs	[bmim][Br] # pairs	# $[H_2O]$ molecules	$\frac{\#[H_2O]}{\#IL}$
Model-A = (0, 100%)	0	250	2919	11.7
Model-B = (25, 75%)	62	188	2921	11.7
Model-C = (50, 50%)	125	125	2930	11.7
Model-D = (75, 25%)	188	62	2927	11.7
Model-E = (100, 0%)	250	0	2940	11.8

In this study, a constant charge density is applied to each electrode, carefully selected to replicate the applied potential. The only charge scaling was applied to the graphene electrodes; fixed surface charge densities σ were imposed to simulate the charged device. Each surface density was converted into an additional atomic charge by dividing the total electrode charge ($\sigma \times S$) by the number of carbon atoms (540 atoms), thereby assigning a uniform supplemental partial charge to each carbon atom. Here, four different fixed charge densities (σ) were applied directly to the carbon electrodes to simulate the SCs: σ = 0.0, 1.6, 3.2, and 4.8 $\mu C/cm^2$. This approach accurately reproduces the applied potential at the electrode−electrolyte interface and follows established methodologies in graphene-based supercapacitor simulations[6,20−22,26,27] and has proven to be accurate for low charge densities that do not result in potential differences greater than approximately 2 V. The electrodes were modeled using parameters based on the OPLS-AA force field.[28] For the electrolytes, the potential models were the same as those used in previous simulations and were also based on the OPLS-AA force field. No scaling of partial charges was applied to the ions ($[bmim]^+$, $[Cl]^-$, and $[Br]^-$), which retained their original OPLS-AA values (refs 28,29). The TIP3P force field[30] was applied to water molecules. These parameters have been widely used for describing electrolyte−electrode interactions and modeling the electrostatic properties of SCs.[6,20−22,26,27] Although the TIP3P water model has well-known limitations—such as overestimating diffusion coefficients and underestimating the dielectric constant of liquid water, its use in this work is justified for two main reasons. First, TIP3P is fully compatible with the OPLS-AA force field employed here to model both the ions and the graphene electrodes. This compatibility ensures parameter consistency and numerical stability throughout the molecular dynamics simulations. Second, the primary objective of this study is to compare different anionic compositions ($[Cl]^-$and $[Br]^-$) under controlled hydration conditions while keeping all other parameters constant. In this context, TIP3P is adequate for capturing relative trends in the structural and electrochemical behavior of the IL/water electrolytes studied without compromising the validity of the conclusions. This approach aligns with several previous studies in the literature that investigated similar systems using a comparative methodology.

To maintain a constant temperature during the MD-NVT simulations, the v-rescale temperature coupling method[31] was used, where particle velocities were rescaled every 0.1 ps. The equations of motion were integrated with a time step of 0.001 ps. The Lennard-Jones (LJ) interactions were calculated using the classical shifted-force technique, while long-range electrostatic corrections were estimated via the particle mesh Ewald (PME) method,[32] applied with a cutoff radius of 1.2 nm. For both LJ and Coulomb interactions, the potential-shift-Verlet modifier was employed. Periodic boundary conditions were applied to all systems under study. Figure 2 shows the initial configurations for SCs with the corresponding compositions for the IL/water mixtures, assembled using the Packmol program.[33] All simulation boxes have the same volume between the two graphene sheets, with dimensions x = 3.707 nm and y = 3.853 nm, and a separation distance of z = 12 nm, resulting in an internal volume of ∼171 nm^3. To prevent interactions between the electrodes, a 48 nm vacuum region was incorporated into the device with 24 nm positioned before the positive electrode and 24 nm after the negative electrode. The simulations were conducted in two stages: (1st) equilibration—aimed at adjusting the system generated by the Packmol program[33] to a thermodynamically equilibrated configuration; this stage was performed for approximately 15 ns. (2nd) Production—intended to generate uncorrelated configurations for statistical analysis; in this stage, 10^8 configurations were produced, resulting in a total of 100 ns of simulation, where 5×10^4 configurations were saved for

https://doi.org/10.1021/acs.jpcc.5c01816
J. Phys. Chem. C 2025, 129, 13532−13541

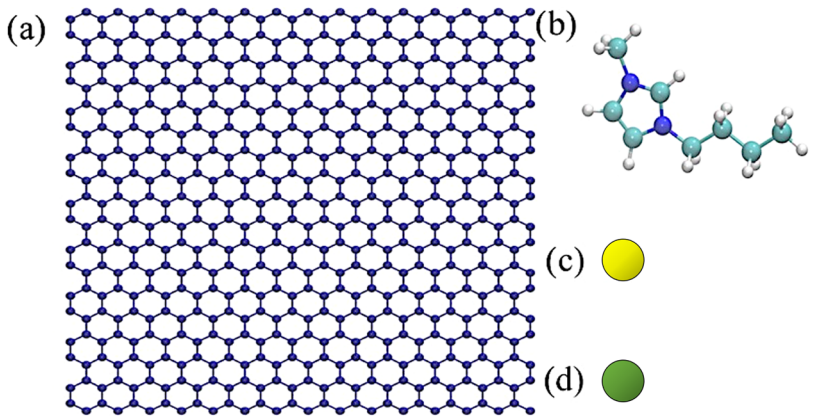

Figure 1. Structures of the (a) graphene electrode and each ionic compound that forms the electrolytes: (b) $[bmim]^+$, (c) $[Br]^-$, and (d) $[Cl]^-$.

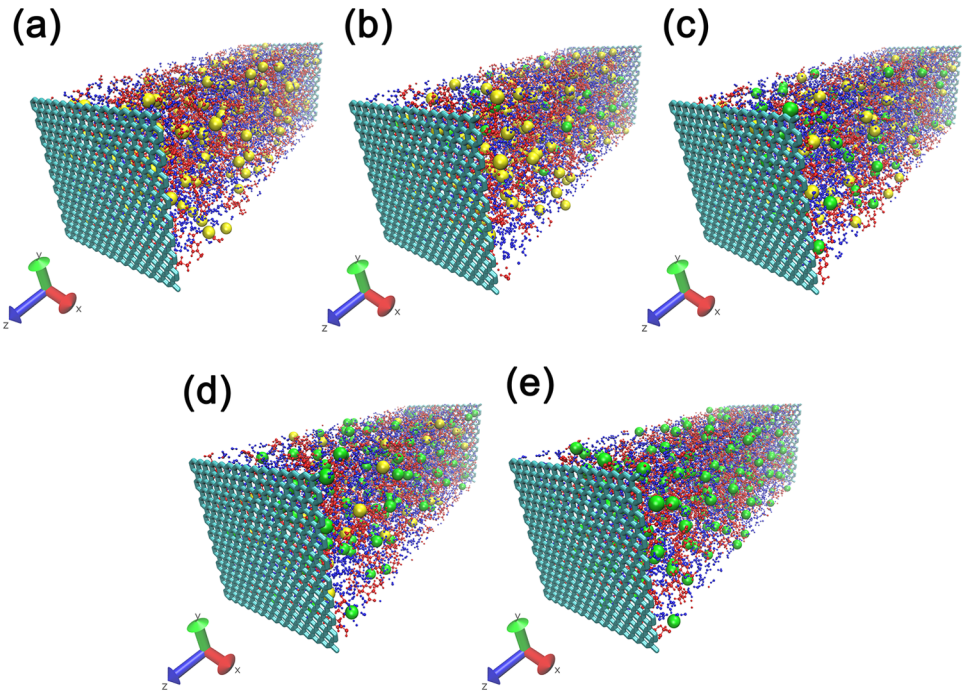

Figure 2. Representation of SCs simulated in this study. Blue grid = carbons (positive and negative electrode); blue molecules = water molecules; red molecules = $[bmim]^+$ ions; yellow circles = $[Br]^-$ ions; green circles = $[Cl]^-$ ions. (a) Model-A, (b) Model-B, (c) Model-C, (d) Model-D, and (e) Model-E.

analysis. All simulations were performed using the Gromacs program.[34] Bond lengths were kept fixed according to the LINCS algorithm.[35] The VMD program was used to visualize the studied systems.[36]

3. RESULTS AND DISCUSSION

3.1. Structural and Energetic Profile of EDL. From a structural and energetic perspective, a detailed understanding of the energy storage process in an SC requires knowledge of the molecular mechanisms underlying the electrical double layer (EDL) formation. Figure 3 presents the mass density profiles (normalized by bulk results) of the ionic species ($[bmim]^+$, $[Cl]^-$, and $[Br]^-$) and water molecules along the SC for the electrolyte composed of Model-C (50, 50%). The results are shown for both the uncharged (σ = 0.0 $\mu C/cm^2$) and charged (σ = 4.8 $\mu C/cm^2$) states of the SC. Comparing the EDL structures of ILs/water in both states reveals that cations and anions form alternating layers extending a few nanometers (<1 nm) from the electrode surfaces. A closer inspection shows that the first adsorbed layer (peak around 24.34 nm) consists of both anionic and cationic species, along with water, adsorbed onto the positive electrode. On the negative electrode (peak around 35.66 nm), only cations and water are adsorbed. The second layer (peak around 24.63 and 35.37 nm) is composed of anions and water, electrostatically attracted to the electrode surface, effectively shielding the first layer. While the interfacial ILs/water structure responds to electrode electrification, variations in $[Cl]^-$ and $[Br]^-$ concentrations have minimal impact on the mass density profiles. For ILs/water electrolytes, the total number of water molecules in the closed system remains constant across the SCs. However, water distribution near the electrodes is asymmetrical, with greater accumulation near the positive electrode surface, regardless of $[Cl]^-$ and $[Br]^-$ concentrations. Figure 3 also shows that the first peak of water mass density occurs within 24.31 nm of the innermost electrode layer,

https://doi.org/10.1021/acs.jpcc.5c01816
J. Phys. Chem. C 2025, 129, 13532−13541

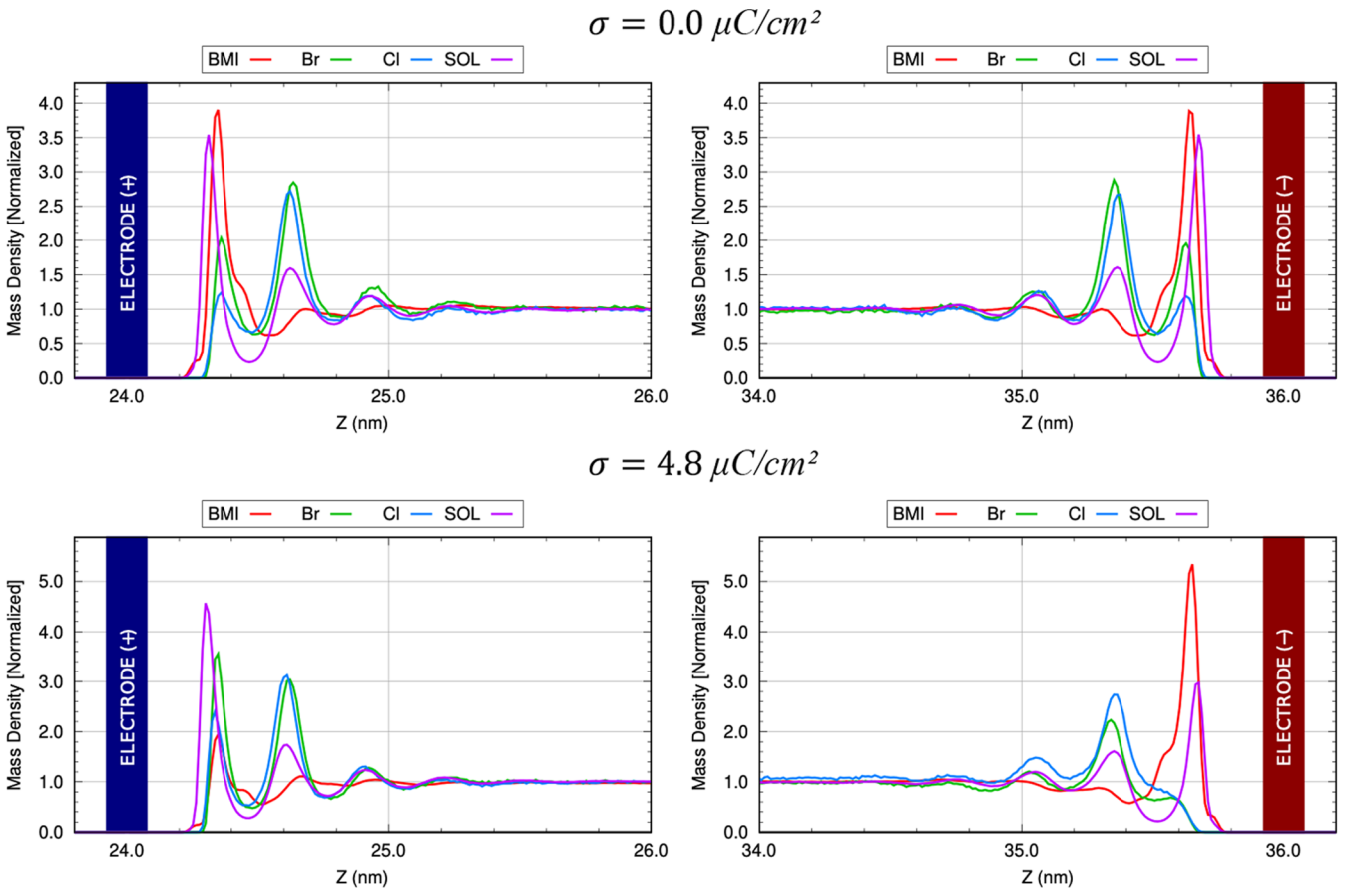

Figure 3. Normalized mass density (kg/m^3) profiles for the components of the electrolyte composed of Model-C (50, 50%) for both uncharged (σ = 0.0 μC/cm^2) and charged (σ = 4.8 μC/cm^2). Water molecules are shown by SOL (solvent). Non-normalized mass density profiles are shown in the Supporting Information (Figure S1).

Table 2. Average Numbers of Each Ionic Component That Forms the Electrolytes in Specific Regions Along the SCs (Rounded Values)[a]

		(a) 0.5 nm			(b) 1.0 nm			(c) 2.0 nm		
$[Cl]^-/[Br]^-$	molecule	EDL$^+$	Bulk	EDL$^-$	EDL$^+$	Bulk	EDL$^-$	EDL$^+$	Bulk	EDL$^-$
Model-A (0, 100%)	$[bmim]^+$	4	235	11	15	214	20	37	171	43
	$[Br]^-$	6	242	2	20	214	17	41	171	38
	H_2O	90	2767	62	221	2509	188	470	2014	436
Model-B (25, 75%)	$[bmim]^+$	4	235	11	15	215	20	37	172	41
	$[Br]^-$	5	182	2	15	161	12	32	129	27
	$[Cl]^-$	1	60	1	4	53	4	9	43	10
	H_2O	91	2767	64	222	2505	194	468	2007	446
Model-C (50, 50%)	$[bmim]^+$	4	235	11	15	215	20	36	172	42
	$[Br]^-$	3	121	1	10	107	7	21	86	18
	$[Cl]^-$	2	122	1	9	107	9	19	86	20
	H_2O	91	2776	63	225	2513	192	476	2013	441
Model-D (75, 25%)	$[bmim]^+$	4	235	11	15	215	20	36	172	42
	$[Br]^-$	2	60	1	5	53	4	11	42	9
	$[Cl]^-$	4	183	2	14	161	12	30	130	28
	H_2O	91	2773	62	224	2511	192	474	2011	443
Model-E (100, 0%)	$[bmim]^+$	4	235	11	15	214	20	37	171	43
	$[Cl]^-$	6	242	2	20	214	17	41	171	38
	H_2O	90	2767	62	221	2509	188	470	2014	436

[a]Each layer corresponds to the cumulative count of particles starting from the electrode. The bulk statistics are calculated from the remaining region containing the electrolyte with a total region of 12 nm. Thus, the particle count is performed up to (a) 0.5 nm of vicinity and 11 nm of bulk; (b) 1 nm of vicinity and 10 nm of bulk; and (c) 2 nm of vicinity and 8 nm of bulk.

https://doi.org/10.1021/acs.jpcc.5c01816
J. Phys. Chem. C 2025, 129, 13532−13541

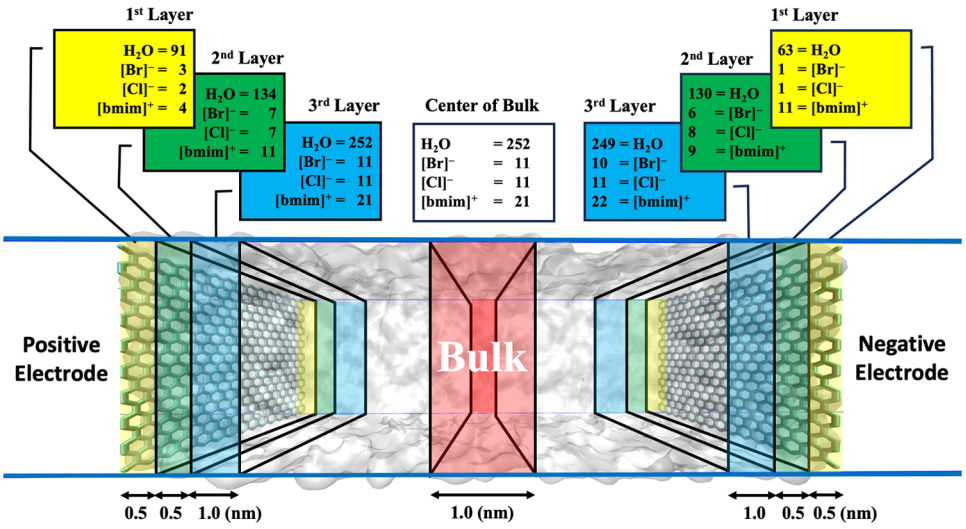

Figure 4. Number of particles in each layer in the vicinity of the positive and negative electrodes of the SC. For comparison, we present the number of particles in a central region of the SC. Note that the third layer within the region near the electrode is similar to that in the bulk region. Analysis was performed for Model-C (50, 50%) proportion of chloride and bromide ions in the electrolyte based on the information described in Table 2.

indicating that water molecules are positioned slightly closer to the electrodes than ionic species and interact directly with them. Furthermore, the peaks in $[Cl]^-$ and $[Br]^-$ density profiles correlate with water density peaks, suggesting that water follows the anion distribution, particularly near positive electrodes where anion density is higher. This suggests that water's asymmetric adsorption results partly from stronger interactions with anions, likely due to more intense hydrogen bonding between anionic species and water in the EDL.

To ensure that our simulations accurately reproduce realistic bulk densities, we have included non-normalized mass density profiles for the IL/water mixtures in the Supporting Information (Figure S1). These non-normalized profiles, presented in the new figure, provide a clear demonstration of the absolute mass densities of the components in the electrolyte. This allows for a more accurate comparison with the experimental data, confirming that our simulations reproduce the bulk density of the system correctly. The density values of the water and ionic species in the bulk region are in good agreement with known experimental densities for similar mixtures. This addition further validates the quality of our force field parameters and confirms the consistency of our simulations in representing the bulk properties of the electrolytes.

We quantified the adsorption of water and ionic species by calculating their average numbers in the first adsorbed layer (within the first 0.50 nm from the electrode). Table 2 presents the average number of each ionic component that makes up the electrolyte, obtained by selecting 5000 configurations from the MD trajectory and identifying specific regions within each configuration, specifically at distances of 0.5, 1.0, and 2.0 nm from the positive and negative electrodes, aiming to quantitatively analyze the variation in the average concentration of ionic species in the positive and negative EDLs. The average numbers of $[bmim]^+$ ions and water molecules adsorbed on each electrode remain essentially constant. At a distance of 0.50 nm, there are approximately 4 (11) $[bmim]^+$ ions near the positive (negative) electrode. For water molecules, the corresponding values range from 90 to 92 (62 to 64). We observed that the number of $[Cl]^-$ and $[Br]^-$ anions adsorbed on the negative electrode is very small compared to that on the positive electrode. There are about 5−6 (2) $[Cl]^-$ and $[Br]^-$ anions near the positive (negative) electrode for different $[Cl]^-/[Br]^-$ concentrations in the electrolyte. These results suggest that anions are not significantly adsorbed on the negative electrode, which is essentially filled with water and $[bmim]^+$, in accordance with the asymmetric distribution of water molecules. At 1 nm (essentially in the EDL), larger amounts of $[bmim]^+$ and water are observed, but their concentrations remain constant on each electrode, while the average number of anions varies with the substitution of $[Br]^-$ by $[Cl]^-$. Table 2 also presents the mean numbers of species at 2 nm from the electrodes. As expected, the differences in the mean numbers of each species at the electrodes decrease and tend toward the bulk values. Figure 4 shows the quantitative distribution of ions and each layer at their corresponding distances from the electrode and at the center of the SC. As observed, the third layer has essentially the same number of ions and water molecules as the center of the SC (bulk).

The asymmetric adsorption of water in the electric double layer (EDL) results partly from stronger interactions with the anions, affecting the water dipole orientation at the electrode surfaces. Water molecules near the positive electrode tend to align such that the negative side of the dipole (oxygen) is attracted to the anions, while the positive side (hydrogens) interacts more with the electrode surface. This alignment leads to greater water accumulation near the positive electrode due to stronger hydrogen-bonding interactions between water and the anions. At the negative electrode, water molecules exhibit a different orientation with less influence from anion interactions, resulting in a more symmetric distribution. This asymmetric water distribution favoring the positive electrode is reflected in the observed density distributions, where water largely follows the anion density, especially near the positive electrode.

Additionally, we present an analysis of the electrostatic charge profiles for the charged SCs (σ = 4.8 $\mu C/cm^2$), shown in Figure 5. As observed, the charge distribution exhibits pronounced oscillations near the electrode surface, gradually

https://doi.org/10.1021/acs.jpcc.5c01816
J. Phys. Chem. C 2025, 129, 13532−13541

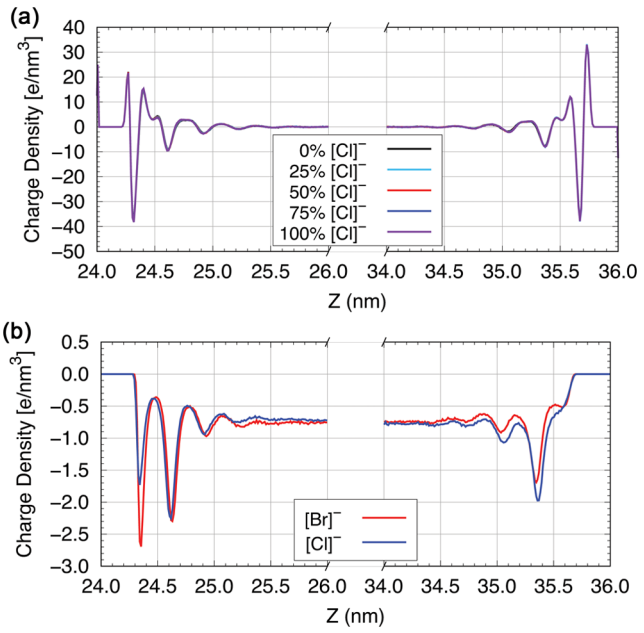

Figure 5. (a) Electrostatic charge profiles along the length of the charged (σ = 4.8 μC/cm^2) SCs by varying $[Cl]^-$ and $[Br]^-$ concentrations; and (b) demonstration of charge density (e/nm^3) for the Model-C (50, 50%) proportion of chloride and bromide ions, highlighting the electrode boundary region.

decreasing across the EDL before stabilizing in the bulk region. This behavior explains the accumulation of ILs/water near highly charged electrodes and suggests that variations in $[Cl]^-$ and $[Br]^-$ concentrations do not impact the device's electrical properties. It is important to highlight that for all studied ion proportions, the results indicate the same total electrostatic charge profile. However, the partial charge for each ion (chloride or bromide) is slightly different, as shown in Figure 5b for the Model-C, proportion (50, 50%), with similar results observed for the other proportions.

To assess how the interactions among ionic species, water, and electrodes influence the ILs/water distribution in the electrode−electrolyte interfacial region, we evaluated the interaction energy per ion or water molecule with the positive and negative electrodes. Figure 6 shows the contributions of the LJ and Coulomb interaction energies for the charged SC (σ = 4.8 μC/cm^2), varying $[Cl]^-$ and $[Br]^-$ concentrations. Overall, the LJ interaction energy is significantly stronger than the Coulomb interaction energy, making it the dominant interaction in ionic species−electrode and water−electrode interactions. Due to its aromatic character and positive charge, $[bmim]^+$ is more strongly attracted to electrodes than anions $[Cl]^-$ and $[Br]^-$, particularly to the negative electrode. We note that both the LJ and Coulomb interaction energies between anions or water molecules and the positive electrode have comparable magnitudes.

3.2. Electric Potential and Capacitance. The electrostatic potential profile along the SC was calculated from MD trajectories using the one-dimensional Poisson equation, as implemented in the Gromacs software package.[34] This profile allows us to extract the potential drop across the positive electrode (Φ^+) and the negative electrode (Φ^-), as well as the total potential drop across the SC ($\Delta\delta\Phi$ = $\Delta\Phi_{charged}-\Delta\Phi_{uncharged}$, $\Delta\Phi=\Phi^+-\Phi^-$). The potential differences were adjusted using the zero-charge potential (PZC) since, for uncharged electrodes, van der Waals interactions between ionic species and water molecules cause a small residual potential difference. The results for Φ^+, Φ^-, $\Delta\Phi$, and $\Delta\delta\Phi$ of ILs/water mixtures are listed in Table 3. The results indicate that as the surface charge density increases, the potential at the positive electrode increases, while the potential at the negative electrode decreases. As expected, variations in $[Cl]^-$ and $[Br]^-$ concentrations have a negligible effect on the potential difference across the device. This trend aligns with the electrostatic charge distribution pattern observed across all considered electrolytes (Figure 5). The electrostatic potential profile derived from the 1D Poisson equation supports the analysis of potential differences across the electrical double layer. These plots are shown in the Supporting Information (Figure S2), allowing a clear visualization of the potential distribution across the electrode−electrolyte interface. Since the potential across the EDL directly influences capacitance,

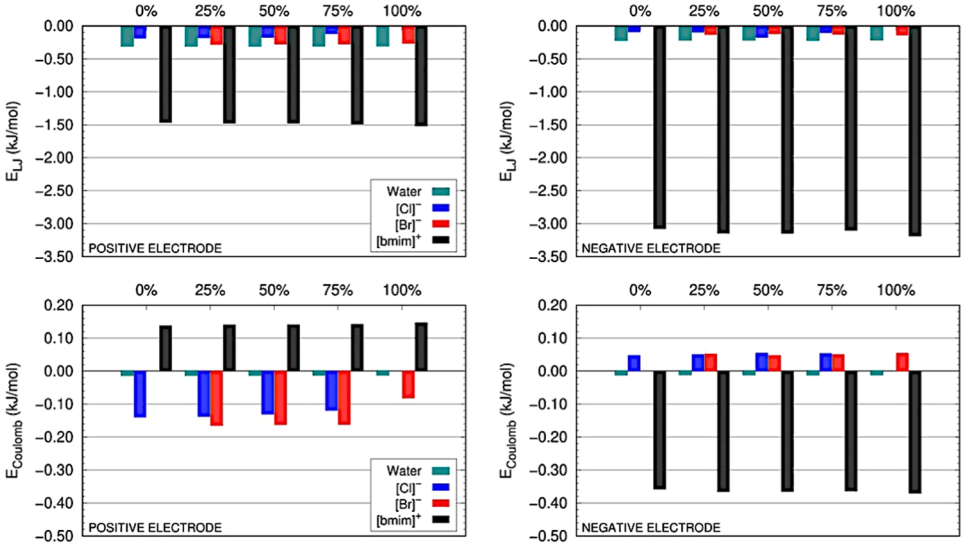

Figure 6. Lennard-Jones and Coulomb interaction energies for the charged SCs (σ = 4.8 μC/cm^2), varying $[Cl]^-$ and $[Br]^-$ concentrations. The percentage in the graph title represents the fraction of bromide in the electrolyte.

https://doi.org/10.1021/acs.jpcc.5c01816
J. Phys. Chem. C 2025, 129, 13532−13541

Table 3. Results for the Electrical Potentials at the Positive Electrode (Φ^+, in V) and the Negative Electrode (Φ^-, in V)[a]

electrolyte	σ	Φ^+	Φ^-	$\Delta\Phi$	$\Delta\delta\Phi$
Model-A (0, 100%)	0.00	0.5674	0.5587	0.0087	0.0087
	1.60	0.8625	0.2553	0.6072	0.5985
	3.20	1.1503	−0.0632	1.2125	1.2038
	4.81	1.4340	−0.3882	1.8222	1.8135
Model-B (25, 75%)	0.00	0.5632	0.5610	0.0022	0.0022
	1.60	0.8700	0.2452	0.6248	0.0623
	3.20	1.1605	0.0746	1.2351	1.2329
	4.81	1.4244	−0.3939	1.8183	1.8161
Model-C (50, 50%)	0.00	0.5687	0.5535	0.0149	0.0149
	1.60	0.8669	0.2421	0.6248	0.6099
	3.20	1.1528	−0.0747	1.2275	1.2126
	4.81	1.4288	−0.4021	1.8309	1.8160
Model-D (75, 25%)	0.00	0.5600	0.5546	0.0054	0.0054
	1.60	0.8636	0.2415	0.6221	0.6167
	3.20	1.1499	−0.0788	1.2287	1.2233
	4.81	1.4315	−0.4026	1.8341	1.8287
Model-E (100, 0%)	0.00	0.5633	0.5533	0.0100	0.0100
	1.60	0.8589	0.2455	0.6134	0.6034
	3.20	1.1454	−0.0835	1.2289	1.2189
	4.81	1.4235	−0.4036	1.8271	1.8171

[a]The potential difference between the electrodes ($\Delta\Phi$, in V) is also provided, along with the total potential difference ($\Delta\delta\Phi$, in V), corrected for the PZC, and σ in $\mu C/cm^2$.

changes in the local anion density also have minimal impact on total capacitance, suggesting that the electrolyte composition remains stable for device performance (Table 4). This stability is particularly beneficial for practical applications, where fluctuations in ion concentration due to evaporation, degradation, or contamination could otherwise affect devise efficiency. The asymmetry in the electrode potentials shown in Table 3 does not stem from differences in surface charge density, which is symmetric in all simulated models. Instead, it arises from asymmetric electrode−electrolyte interactions. Although the applied charges are equal, ionic distributions and electrostatic interactions differ on each side of the EDL, leading to distinct potential profiles. Stronger anion−water interactions at the positive electrode cause greater water accumulation, while the negative electrode shows more symmetric adsorption. This charge reorganization within the EDL results in observed potential asymmetry.

Table 4. Results for the Capacitances (in $\mu F/cm^2$) of the Positive and Negative Electrodes (Given by $C^+ = \sigma^+/\Phi^+$ and $C^- = \sigma^-/\Phi^-$), As Well As the Total Capacitance (Given by $C_{Tot} = (C^- C^+)/(C^- + C^+)$) of the SCs, and σ in $\mu C/cm^2$

electrolyte	σ	C^+	C^-	C_{Tot}	$\overline{C_{Tot}}$
Model-A (0, 100%)	1.60	1.8574	−6.2750	2.6383	2.639 ± 0.003
	3.20	2.7854	51.5113	2.6425	
	4.81	3.3515	12.3802	2.6375	
Model-B (25, 75%)	1.60	1.8414	−6.5334	2.5640	2.600 ± 0.040
	3.20	2.7609	42.9491	2.5941	
	4.81	3.3741	12.2011	2.6431	
Model-C (50, 50%)	1.60	1.8480	−6.6171	2.5640	2.600 ± 0.032
	3.20	2.7793	42.8916	2.6102	
	4.81	3.3637	11.9523	2.6249	
Model-D (75, 25%)	1.60	1.8550	−6.6335	2.5751	2.601 ± 0.023
	3.20	2.7863	40.6599	2.6076	
	4.81	3.3573	11.9374	2.6204	
Model-E (100, 0%)	1.60	1.8652	−6.5255	2.6117	2.616 ± 0.012
	3.20	2.7973	38.3713	2.6072	
	4.81	3.3762	11.9078	2.6304	

From Table 4, we note that the magnitude of the electrode capacitances is particularly affected by the variation of the electric potential with charge density and the estimates of C^+ and C^- (given by $C^+ = \sigma^+/\Phi^+$ and $C^- = \sigma^-/\Phi^-$). It may contain variations due to the sensitivity in obtaining the electric potential value and therefore may not be entirely suitable to definitively characterize this property of the SC. On the other hand, for all electrolytes, a linear relationship is observed between Φ and σ, with slopes numerically equal to the negative and positive capacitances of the electrodes, of C^+ and C^-. These capacitances can be combined in series to determine the total capacitance of the SC, given by $C_{Tot} = (C^- C^+)/(C^- + C^+)$. Figure 7 illustrates this relationship for the electrolyte Model-C (50, 50%). The electrode capacitance values obtained through linear regression along with the total capacitance of the SCs are presented in Table 5. The results indicate that the capacitance of the positive electrode is approximately 10% higher than that of the negative electrode. As expected, variations in the concentrations of $[Cl]^-$ and $[Br]^-$ do not significantly affect the capacitance of each electrode. For Model-C, the linear regression results for C^- and C^+ are 5.04 and 5.59 $\mu F/cm^2$, respectively, and for C_{Tot}, it is 2.65 $\mu F/cm^2$. For comparison, the capacitance values (C^-, C^+, and C_{Tot}) of graphene-based SCs composed of 1-ethyl-3-methylimidazolium tetrafluoroborate ($[emim]^+$ and $[BF_4]^-$) and choline-glycine ($[cho]^+$ and $[gly]^-$), with 60% hydration, are 5.30, 5.04, and 2.56 $\mu F/cm^2$ and 5.42, 4.94, and 2.58 $\mu F/cm^2$, respectively.[6]

3.3. Electrochemical Energy Storage. The ability of SCs to store energy is a critical aspect of their function and depends on the hydration level of the electrolyte. Using potential difference (Table 3) and total capacitance (Table 4) values, we calculated gravimetric energy densities of each device using $u_m = C_{Tot}(\Delta\delta\Phi)^2/2m$, where m is the mass of the SC. In Table 6, we present a first estimate for the u_m values obtained for electrolytes with 60% hydration. For comparison, the table also includes the corresponding volumetric energy densities. Unlike electrical properties, increasing the concentration of $[Cl]^-$ systematically increases the gravimetric energy density. The electrolyte with 100% $[Cl]^-$ (Model-E) exhibits an approximately 10% increase in energy density compared to the electrolyte with 100% $[Br]^-$ (Model-A) for σ = 4.8 $\mu C/cm^2$ (~1.82 V). We also analyzed energy storage capabilities in electrolytes with fewer water molecules. We considered electrolytes with 534 pairs of [bmim][Br] ([bmim][Cl]) and 1013 (1028) water molecules, corresponding to approximately 10% hydration. MD results show that reducing mass by replacing $[Br]^-$ by $[Cl]^-$ does not compromise overall electrochemical performance, with $\Delta\delta\Phi$ of 2.01 (1.87) V and a corresponding C_{Tot} of 2.42 (2.53) $\mu F/cm^2$ for σ = 4.8 $\mu C/cm^2$ on the electrode. However, at 10% hydration, the gravimetric energy density (3.05 J/g, at 1.87 V) for [bmim][Cl]+1028 water molecules decreases by 12%, indicating reduced storage capacity when compared to devices at 60% hydration (3.41 J/g, at 1.82 V). These findings highlight that increasing the level of hydration enhances the gravimetric efficiency of [bmim]([Br]/[Cl])-based SCs.

https://doi.org/10.1021/acs.jpcc.5c01816
J. Phys. Chem. C 2025, 129, 13532−13541

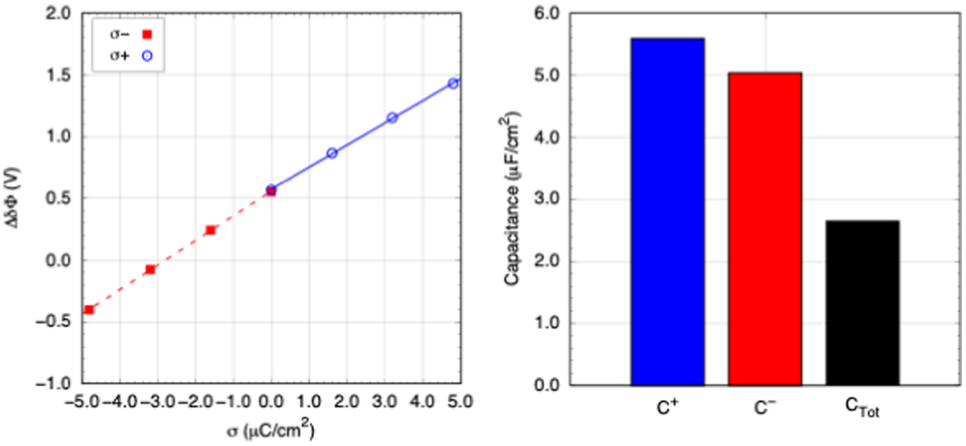

Figure 7. Linear regression of the electrical potential results for the positive (C^+) and negative (C^-) electrodes as a function of charge density for Model-C (50, 50%). Results for C^+, C^-, and C_{Tot} are also presented.

Table 5. Linear Regression Results for the Capacitances of the Positive (C^+, in $\mu F/cm^2$) and Negative (C^-, in $\mu F/cm^2$) Electrodes, As Well As the Total Capacitance (C_{Tot}, in $\mu F/cm^2$) of the SCs

electrolyte	C^-	C^+	C_{Tot}
Model-A (0, 100%)	5.01	5.59	2.64
Model-B (25, 75%)	5.02	5.53	2.63
Model-C (50, 50%)	5.04	5.59	2.65
Model-D (75, 25%)	5.28	5.58	2.71
Model-E (100, 0%)	5.07	5.55	2.65

Table 6. Volumetric and Gravimetric Energy Densities Obtained with Varying $[Cl]^-$ and $[Br]^-$ Concentrations

electrolyte	σ ($\mu C/cm^2$)	u_v (J/cm^3)	u_m (J/g)
Model-A (0, 100%)	1.60	0.39	0.34
	3.20	1.60	1.37
	4.81	3.61	3.10
Model-B (25, 75%)	1.60	0.41	0.36
	3.20	1.64	1.44
	4.81	3.63	3.19
Model-C (50, 50%)	1.60	0.40	0.36
	3.20	1.60	1.44
	4.81	3.61	3.24
Model-D (75, 25%)	1.60	0.41	0.38
	3.20	1.63	1.50
	4.81	3.65	3.36
Model-E (100, 0%)	1.60	0.40	0.37
	3.20	1.61	1.52
	4.81	3.62	3.41

To accurately compare the efficiency of these devices, they must be evaluated under the same potential difference. Therefore, we performed a quadratic fit of the gravimetric energy density as a function of the potential difference to assess the SC performance. Figure 8 presents the projected energy density for an electrical value of 2.0 V [bmim]([Br]/[Cl])-based SCs with 60% hydration, which exhibit higher gravimetric energy storage efficiency. The projected energy density results for a fixed potential difference of 2.0 V are summarized in Table 7. The projected results also indicate an ∼9% increase in energy density for Model-E relative to Model-A electrolyte. Therefore, optimizing electrolyte composition to increase the gravimetric energy density without compromising the electrochemical performance has significant practical implications. This is particularly beneficial for portable electronics, electric vehicles, and aerospace applications where weight constraints are crucial.

4. CONCLUSIONS

In this study, we investigated the impact of varying chloride and bromide concentrations in ionic liquid (IL)/water electrolytes on the electrochemical performance of graphene-based SCs by using atomistic MD simulations. Our findings indicate that while changes in anion composition have a negligible effect on electrostatic charge distribution and capacitance, they significantly influence the gravimetric energy density of the device. Specifically, increasing the $[Cl]^-$ concentration leads to a systematic enhancement in energy storage capacity, with an approximate 10% increase in gravimetric energy density. Additionally, our analysis of the EDL structure shows that water molecules preferentially accumulate near positive electrodes following anion distribution. The interaction energy analysis confirms that water−electrode interactions, particularly with anions, play a key role in determining the interfacial electrolyte organization. Furthermore, we examined the influence of hydration levels and found that higher water content improves the gravimetric efficiency of IL/water-based SCs, highlighting the importance of electrolyte composition in optimizing the energy storage performance. Our results show a consistent increase in gravimetric energy density with higher [bmim][Cl] content in the electrolyte. However, chloride-based ionic liquids typically have higher viscosity than their bromide-based counterparts.[37] This effect is more pronounced in concentrated solutions, but under the simulated conditions (∼60% hydration), the high water content significantly reduces the viscosity. Water as a cosolvent improves ionic mobility and prevents slow charging. Still, viscosity remains a key factor in practical applications and should be considered in future studies, especially under more concentrated or low-hydration conditions. Overall, our results suggest that tuning the anion composition in IL/water electrolytes provides a viable strategy for enhancing SC performance without compromising electrochemical stability. These insights are particularly relevant for applications where weight reduction, high efficiency, and cost-effectiveness are critical.

https://doi.org/10.1021/acs.jpcc.5c01816
J. Phys. Chem. C 2025, 129, 13532−13541

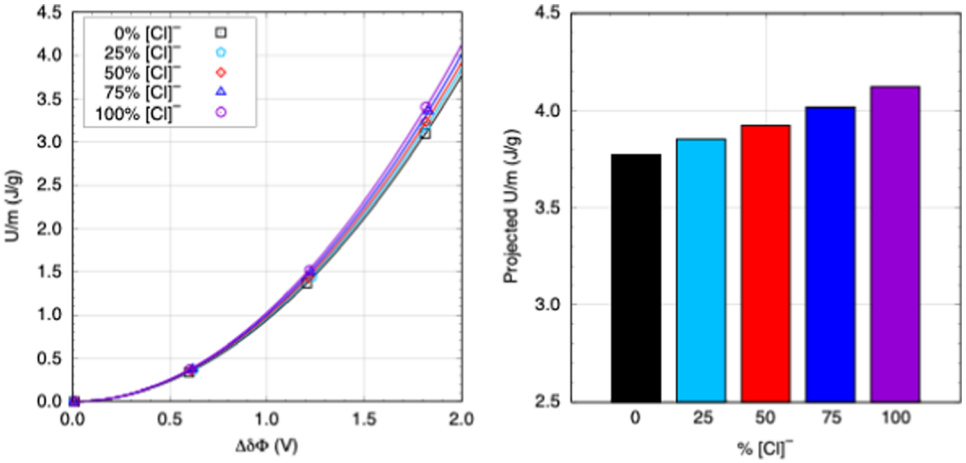

Figure 8. (Left) Projection of the gravimetric energy density in terms of the potential difference varying the $[Cl]^-$ concentration in the electrolyte. (Right) Total energy stored per mass for each studied model.

Table 7. Results for the Projected Energy Density for a Potential Difference of 2.0 V, Which Is Held Fixed

electrolyte	u_m (J/g)
Model-A (0, 100%)	3.77
Model-B (25, 75%)	3.85
Model-C (50, 50%)	3.92
Model-D (75, 25%)	4.02
Model-E (100, 0%)	4.12

■ ASSOCIATED CONTENT

Supporting Information

The Supporting Information is available free of charge at https://pubs.acs.org/doi/10.1021/acs.jpcc.5c01816.

The unnormalized mass density profiles and the electric potential profiles (PDF)

Molecular dynamics simulation files, including input and output files for the supercapacitor configurations, force field files, and data structure files required for simulations using the GROMACS software (ZIP)

■ AUTHOR INFORMATION

Corresponding Author

Guilherme Colherinhas − *Instituto de Física, Universidade Federal de Goiás, Goiânia, Goiás 74690-900, Brasil;* orcid.org/0000-0002-4526-3408; Email: gcolherinhas@ufg.br

Authors

Leonardo B. A. Oliveira − *Departamento de Física, CEPAE, Universidade Federal de Goiás, Goiânia, Goiás 74690-900, Brasil*

Lucas de S Silva − *Instituto de Física, Universidade Federal de Goiás, Goiânia, Goiás 74690-900, Brasil;* orcid.org/0009-0002-0539-1103

Henrique de Araujo Chagas − *Instituto de Física, Universidade Federal de Goiás, Goiânia, Goiás 74690-900, Brasil;* orcid.org/0000-0002-7696-010X

Tertius L. Fonseca − *Instituto de Física, Universidade Federal de Goiás, Goiânia, Goiás 74690-900, Brasil;* orcid.org/0000-0001-5501-7801

Complete contact information is available at: https://pubs.acs.org/10.1021/acs.jpcc.5c01816

Funding

The Article Processing Charge for the publication of this research was funded by the Coordenacao de Aperfeicoamento de Pessoal de Nivel Superior (CAPES), Brazil (ROR identifier: 00x0ma614).

Notes

The authors declare no competing financial interest.

■ ACKNOWLEDGMENTS

This work was supported by research grants from Conselho Nacional de Desenvolvimento Científico e Tecnológico—CNPq, Fundação de Amparo à Pesquisa do Estado de Goiás—FAPEG, and Coordenação de Aperfeiçoamento de Pessoal de Nível Superior—CAPES.

■ REFERENCES

(1) Simon, P.; Gogotsi, Y. Materials for Electrochemical Capacitors. *Nat. Mater.* **2008**, *7* (11), 845−854.

(2) Salanne, M.; Rotenberg, B.; Naoi, K.; Kaneko, K.; Taberna, P.-L.; Grey, C. P.; Dunn, B.; Simon, P. Efficient Storage Mechanisms for Building Better Supercapacitors. *Nat. Energy* **2016**, *1* (6), No. 16070.

(3) Simon, P.; Gogotsi, Y. Perspectives for Electrochemical Capacitors and Related Devices. *Nat. Mater.* **2020**, *19* (11), 1151−1163.

(4) Shao, Y.; El-Kady, M. F.; Sun, J.; Li, Y.; Zhang, Q.; Zhu, M.; Wang, H.; Dunn, B.; Kaner, R. B. Design and Mechanisms of Asymmetric Supercapacitors. *Chem. Rev.* **2018**, *118* (18), 9233−9280.

(5) Malaspina, T.; Colherinhas, G.; Weitzner, S. E.; Wood, B. C.; Fileti, E. E. Ab Initio Dynamics of Graphene and Graphyne Electrodes in Vacuum and in the Presence of Electrolytes. *J. Phys. Chem. C* **2023**, *127* (13), 6515−6523.

(6) de Araujo Chagas, H.; Oliveira, L. B. A.; Fonseca, T. L.; Colherinhas, G. Systematic Analysis to Evaluate the Impact of Hydration on Electrolytes [Emim][BF4] and [Cho][Gly] in Supercapacitors Formed by Graphene or Graphyne Electrodes. *J. Mol. Liq.* **2024**, *415*, No. 126280.

(7) Hallett, J. P.; Welton, T. Room-Temperature Ionic Liquids: Solvents for Synthesis and Catalysis. 2. *Chem. Rev.* **2011**, *111* (5), 3508−3576.

(8) Maton, C.; De Vos, N.; Stevens, C. V. Ionic Liquid Thermal Stabilities: Decomposition Mechanisms and Analysis Tools. *Chem. Soc. Rev.* **2013**, *42* (13), No. 5963.

(9) Fedorov, M. V.; Kornyshev, A. A. Ionic Liquids at Electrified Interfaces. *Chem. Rev.* **2014**, *114* (5), 2978−3036.

(10) Hayes, R.; Warr, G. G.; Atkin, R. Structure and Nanostructure in Ionic Liquids. *Chem. Rev.* **2015**, *115* (13), 6357−6426.

(11) Watanabe, M.; Thomas, M. L.; Zhang, S.; Ueno, K.; Yasuda, T.; Dokko, K. Application of Ionic Liquids to Energy Storage and Conversion Materials and Devices. *Chem. Rev.* **2017**, *117* (10), 7190−7239.
(12) Armand, M.; Endres, F.; MacFarlane, D. R.; Ohno, H.; Scrosati, B. Ionic-Liquid Materials for the Electrochemical Challenges of the Future. *Nat. Mater.* **2009**, *8* (8), 621−629.
(13) Bruno Assis Oliveira, L.; Fonseca, T. L.; Colherinhas, G. Investigating Ionic Liquid Hydration Effects at High Temperatures: Insights from Classic Molecular Dynamics Simulations. *J. Mol. Liq.* **2024**, *393*, No. 123662.
(14) Feng, G.; Jiang, X.; Qiao, R.; Kornyshev, A. A. Water in Ionic Liquids at Electrified Interfaces: The Anatomy of Electrosorption. *ACS Nano* **2014**, *8* (11), 11685−11694.
(15) Suo, L.; Borodin, O.; Gao, T.; Olguin, M.; Ho, J.; Fan, X.; Luo, C.; Wang, C.; Xu, K. Water-in-Salt" Electrolyte Enables High-Voltage Aqueous Lithium-Ion Chemistries. *Science (1979)* **2015**, *350* (6263), 938−943.
(16) Zheng, J.; Tan, G.; Shan, P.; Liu, T.; Hu, J.; Feng, Y.; Yang, L.; Zhang, M.; Chen, Z.; Lin, Y.; Lu, J.; Neuefeind, J. C.; Ren, Y.; Amine, K.; Wang, L.-W.; Xu, K.; Pan, F. Understanding Thermodynamic and Kinetic Contributions in Expanding the Stability Window of Aqueous Electrolytes. *Chem.* **2018**, *4* (12), 2872−2882.
(17) Qiao, R. Water at Ionic Liquids-Solid Interfaces. *Curr. Opin Electrochem* **2019**, *13*, 11−17.
(18) Chen, M.; Wu, J.; Ye, T.; Ye, J.; Zhao, C.; Bi, S.; Yan, J.; Mao, B.; Feng, G. Adding Salt to Expand Voltage Window of Humid Ionic Liquids. *Nat. Commun.* **2020**, *11* (1), No. 5809.
(19) Zhou, A.; Zhang, J.; Chen, M.; Yue, J.; Lv, T.; Liu, B.; Zhu, X.; Qin, K.; Feng, G.; Suo, L. An Electric-Field-Reinforced Hydrophobic Cationic Sieve Lowers the Concentration Threshold of Water-In-Salt Electrolytes. *Adv. Mater.* **2022**, *34* (47), No. 2207040, DOI: 10.1002/adma.202207040.
(20) de S Silva, L.; de A Chagas, H.; Colherinhas, G. Sustainable Supercapacitors Using Advanced Hydrated Amino Acid Ionic Liquids: A Novel Approach to Biodegradable Energy Storage. *J. Mol. Liq.* **2025**, *417*, No. 126638.
(21) de Araujo Chagas, H.; Fileti, E. E.; Colherinhas, G. A Molecular Dynamics Study of Graphyne-Based Electrode and Biocompatible Ionic Liquid for Supercapacitor Applications. *J. Mol. Liq.* **2022**, *360*, No. 119494.
(22) de Araujo Chagas, H.; Fileti, E. E.; Colherinhas, G. Comparing Supercapacitors with Graphene/Graphyne Electrodes and [Bmim]-[PF6], [Emim][BF4], [Ch][Gly] and [Pyr][Tfsi] Ionic Liquids Using Molecular Dynamics. *J. Mol. Liq.* **2023**, *379*, No. 121703.
(23) Spickermann, C.; Thar, J.; Lehmann, S. B. C.; Zahn, S.; Hunger, J.; Buchner, R.; Hunt, P. A.; Welton, T.; Kirchner, B. Why Are Ionic Liquid Ions Mainly Associated in Water? A Car−Parrinello Study of 1-Ethyl-3-Methyl-Imidazolium Chloride Water Mixture. *J. Chem. Phys.* **2008**, *129* (10), No. 104505, DOI: 10.1063/1.2974098.
(24) Remsing, R. C.; Liu, Z.; Sergeyev, I.; Moyna, G. Solvation and Aggregation of *N,N′* -Dialkylimidazolium Ionic Liquids: A Multinuclear NMR Spectroscopy and Molecular Dynamics Simulation Study. *J. Phys. Chem. B* **2008**, *112* (25), 7363−7369.
(25) D'Angelo, P.; Serva, A.; Aquilanti, G.; Pascarelli, S.; Migliorati, V. Structural Properties and Aggregation Behavior of 1-Hexyl-3-Methylimidazolium Iodide in Aqueous Solutions. *J. Phys. Chem. B* **2015**, *119* (45), 14515−14526.
(26) Fileti, E. E.; Colherinhas, G. Investigating the Asymmetry in the EDL Response of C60/Graphene Supercapacitors. *Phys. Chem. Chem. Phys.* **2019**, *21* (28), 15362−15371.
(27) Neto, A. J. P.; Fileti, E. E. Differential Capacitance and Energetics of the Electrical Double Layer of Graphene Oxide Supercapacitors: Impact of the Oxidation Degree. *J. Phys. Chem. C* **2018**, *122* (38), 21824−21832.
(28) Jorgensen, W. L.; Maxwell, D. S.; Tirado-Rives, J. Development and Testing of the OPLS All-Atom Force Field on Conformational Energetics and Properties of Organic Liquids. *J. Am. Chem. Soc.* **1996**, *118* (45), 11225−11236.
(29) Chaban, V. V.; Voroshylova, I. V.; Kalugin, O. N.; Prezhdo, O. V. Acetonitrile Boosts Conductivity of Imidazolium Ionic Liquids. *J. Phys. Chem. B* **2012**, *116* (26), 7719−7727.
(30) Jorgensen, W. L.; Chandrasekhar, J.; Madura, J. D.; Impey, R. W.; Klein, M. L. Comparison of Simple Potential Functions for Simulating Liquid Water. *J. Chem. Phys.* **1983**, *79* (2), 926−935.
(31) Bussi, G.; Donadio, D.; Parrinello, M. Canonical Sampling through Velocity Rescaling. *J. Chem. Phys.* **2007**, *126* (1), No. 014101.
(32) Darden, T.; York, D.; Pedersen, L. Particle Mesh Ewald: An N·log(N) Method for Ewald Sums in Large Systems. *J. Chem. Phys.* **1993**, *98* (12), 10089−10092.
(33) Martínez, L.; Andrade, R.; Birgin, E. G.; Martínez, J. M. PACKMOL: A Package for Building Initial Configurations for Molecular Dynamics Simulations. *J. Comput. Chem.* **2009**, *30* (13), 2157−2164.
(34) Abraham, M. J.; Murtola, T.; Schulz, R.; Páll, S.; Smith, J. C.; Hess, B.; Lindah, E. Gromacs: High Performance Molecular Simulations through Multi-Level Parallelism from Laptops to Supercomputers. *SoftwareX* **2015**, *1−2*, 19−25.
(35) Hess, B.; Bekker, H.; Berendsen, H. J. C.; Fraaije, J. G. E. M. LINCS: A Linear Constraint Solver for Molecular Simulations. *J. Comput. Chem.* **1997**, *18* (12), 1463−1472.
(36) Humphrey, W.; Dalke, A.; Schulten, K. VMD: Visual Molecular Dynamics. *J. Mol. Graph* **1996**, *14* (1), 33−38.
(37) Liu, W.; Cheng, L.; Zhang, Y.; Wang, H.; Yu, M. The Physical Properties of Aqueous Solution of Room-Temperature Ionic Liquids Based on Imidazolium: Database and Evaluation. *J. Mol. Liq.* **2008**, *140* (1−3), 68−72.